

PAPER

## Three-dimensional plasma actuation for faster transition to turbulence

To cite this article: Arnob Das Gupta and Subrata Roy 2017 *J. Phys. D: Appl. Phys.* **50** 425201

View the [article online](#) for updates and enhancements.

### Related content

- [Arc reattachment driven by a turbulent boundary layer: implications for the sweeping of lightning arcs along aircraft](#)  
C Guerra-Garcia, N C Nguyen, J Peraire et al.
- [Reynolds number effects on the fluctuating velocity distribution in wall-bounded shear layers](#)  
Wenfeng Li, Dorothee Roggenkamp, Wilhelm Jessen et al.
- [Direct numerical simulation of spatially developing turbulent boundary layers with opposition control](#)  
Qian-Jin Xia, Wei-Xi Huang, Chun-Xiao Xu et al.

# Three-dimensional plasma actuation for faster transition to turbulence

Arnob Das Gupta  and Subrata Roy 

Department of Mechanical and Aerospace Engineering, Applied Physics Research Group, University of Florida, Gainesville, FL 32611, United States of America

E-mail: [roy@ufl.edu](mailto:roy@ufl.edu)

Received 29 May 2017, revised 10 August 2017

Accepted for publication 25 August 2017

Published 22 September 2017



CrossMark

## Abstract

We demonstrate that a 3D non-linear plasma actuation method creates secondary instabilities by forming lambda vortices for a spatially developing turbulent boundary layer flow over a flat plate. Both bypass transition and controlled transition processes are numerically investigated using wall resolved modal discontinuous Galerkin based implicit large eddy simulation. The largest momentum thickness based Reynolds numbers ( $Re_\theta$ ) tested are 1250 and 1100 for the bypass transition and the controlled transition, respectively. The 3D actuation method is based on a square serpentine plasma actuator (Durscher and Roy 2012 *J. Phys. D: Appl. Phys.* **45** 035202). The transition is achieved via oblique wave transition by perturbing the flow at a frequency of 1 kHz with amplitude of 10% of the freestream velocity. Although the flow is perturbed at a single frequency, the instabilities arising due to the nonlinear interaction between the consecutive lambda vortices, creates subharmonic lambda vortices (half of the fundamental frequency), which finally break down into fully turbulent flow. These interactions have been thoroughly studied and discussed. Since the actuation creates oblique wave transition it will allow faster transition compared to the standard secondary instability mechanism with similar disturbance amplitude reducing the amount of energy input required for flow control.

Keywords: serpentine plasma actuator, transition to turbulence, secondary instabilities, oblique transition

(Some figures may appear in colour only in the online journal)

## 1. Introduction

Turbulent flow over a flat plate has been extensively studied both experimentally and numerically in order to understand the fluid–fluid and fluid–structure interactions in various applications. The main objective, has been to obtain better scaling laws and models for predicting quantities of practical relevance. Extensive experimental studies of the turbulent boundary layer have been conducted [2–9]. Degraaff and Eaton [7] provided data for a wide range of Reynolds numbers and different scaling parameters for predicting boundary layer characteristics at near wall and wake region. Hutchins *et al* [9] conducted studies on large scale coherent structures for atmospheric turbulence and compared them with the laboratory turbulent boundary layers. They found that the two-point correlation of velocity fluctuations are similar for both cases.

In practical applications, the Reynolds numbers  $Re_L = U_\infty L / \nu$  based on freestream velocity  $U_\infty$ , characteristic length  $L$ , and kinematic viscosity  $\nu$ , can go up to  $O(10^8)$ . This is challenging to obtain in laboratory experiments or simulation settings due to large length scales and prohibitive computational resource requirement. Therefore, better scaling laws and sub-grid stress models are required to predict turbulent flowfield at high Reynolds numbers. Due to the recent advances in computational technology, direct numerical simulation (DNS) has become feasible for simulating zero pressure gradient turbulent boundary layer (ZPGTBL) at moderate Reynolds numbers. DNS for spatially developing ZPGTBL was conducted by Spalart [10] for Reynolds number based on momentum thickness  $\theta$  ( $Re_\theta = U_\infty \theta / \nu$ ) up to 1410 and by Schlatter [8] for  $Re_\theta$  up to 2500, which gave extensive benchmark data for this problem. Although DNS is a useful

**Table 1.** Computational mesh details.

		$N_x$	$N_y$	$N_z$	$\Delta x_i^+$	$\Delta y_i^+$	$\Delta z_i^+$	$L_x^+$	$L_y^+$	$L_z^+$
Case I	Coarse	700	48	32	26.5	0.9	24	18600	4200	750
	z_fine	700	48	64	26.5	0.9	12	18600	4200	750
	Medium	700	64	64	26.5	0.9	12	18600	4200	750
	Fine	950	96	64	13	0.9	12	18600	4200	750
Case II		750	64	64	26	0.9	11	20000	2950	750

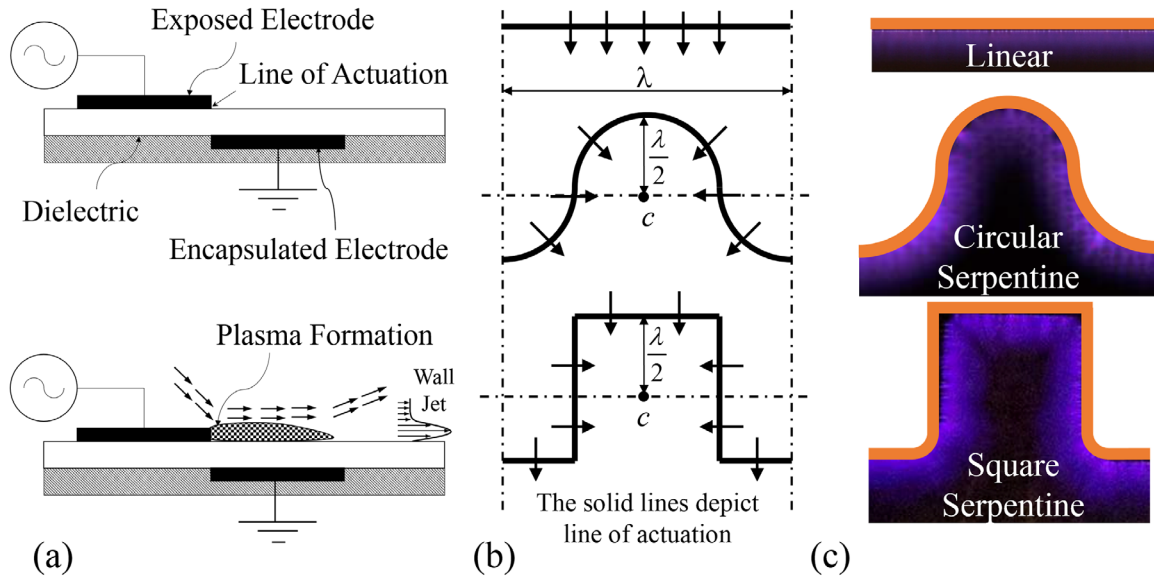


**Figure 1.** (a) Schematic of the operation of SDBD actuator and plasma formation, (b) different geometries of the plasma actuator depending on the shape of line of actuation and (c) formation of plasma around different electrode geometries at 14 kV<sub>pp</sub> and 1 kHz.

tool to accurately capture all the relevant scales in a flow of moderate Reynolds number, computational resource demands remain restrictive. As a remedy, large-eddy simulations (LES) have become increasingly popular as a simulation tool to understand turbulent flow physics. It is based on a low pass filtering operation which acts as a sub-grid scale model for the small-scale structures with high frequencies and allows turbulent simulations to be practicable. Various sub-grid scale models have been studied in literature [11–15]. For detailed information on different LES modelling techniques and trends the author refers the reader to the book by Lesieur *et al* [16]. Although extensive research has been done in order to model the small-scale structures, a universal SGS model is yet to be found.

In the present work the turbulent flow simulations have been carried out using implicit large eddy simulation (ILES) with a modal discontinuous Galerkin (DG) method. The ILES approach [17] does not require problem specific description of SGS model. The use of shock capturing schemes for ILES has been discussed by Garnier *et al* [18]. The numerics of ILES is based on modified equation analysis [19]. For ILES, the truncation terms due to the numerical algorithm have similar properties as the SGS models [17]. Examples of methods used for ILES are flux corrected transport, piecewise parabolic method [20] and multi-dimensional positive definite advection transport algorithm [21]. In this paper ZPGTBL is studied using wall resolved DG ILES, in order to investigate the inherent turbulent flow physics. A validation study has also been provided

using a well-documented tripping mechanism [22] for the ZPGTBL. The first representative set of works on LES using DG was conducted by Collis and Chang [23]. They studied flow over a cylinder and inside a channel. Sengupta *et al* [24] and Wei and Pollard [25] simulated turbulent channel flow using DG method. More recently [26–29], conducted simulation of turbulent flow over an airfoil. DG method was also tested for different types of problems including isotropic turbulence and channel flow [30].

This paper investigates spatially developing ZPGTBL using bypass mechanism provided by Schlatter and Orlu [22] as a benchmarking study. Also, the effect of 3D plasma actuation on a laminar boundary layer is examined. The geometry and forcing details of the actuator are provided in section 2.3. The 3D actuation method relies on the effects similar to that of a square serpentine surface dielectric barrier discharge (SDBD) plasma actuator [1]. Plasma actuators have been studied extensively, as a flow control device over the past few decades [31–34]. Numerical and experimental studies have shown plasma actuators can be used to either suppress [35–37] or raise [38, 39] the growth of Tollmien–Schlichting (TS) waves and thereby delaying or advancing the transition to turbulence. The transition can be manipulated by applying actuators at different locations and voltages [35]. The present study investigates the effect of pulsed actuation as a destabilizing mechanism, for transitioning the flow from laminar to turbulence, directly via secondary instabilities. A study of the interaction between the structures generated by the actuator

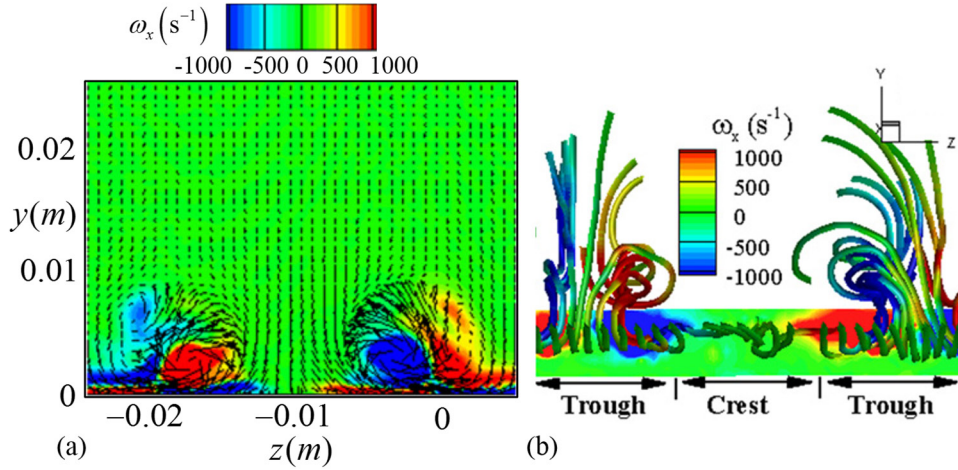


**Figure 2.** (a) Time averaged contours of streamwise oriented bound vortical structures on a  $y$ - $z$  plane 12.5 mm from the beginning of the actuator and (b) corkscrew like structures of streamtraces colored with vorticity induced by square serpentine actuators [1].

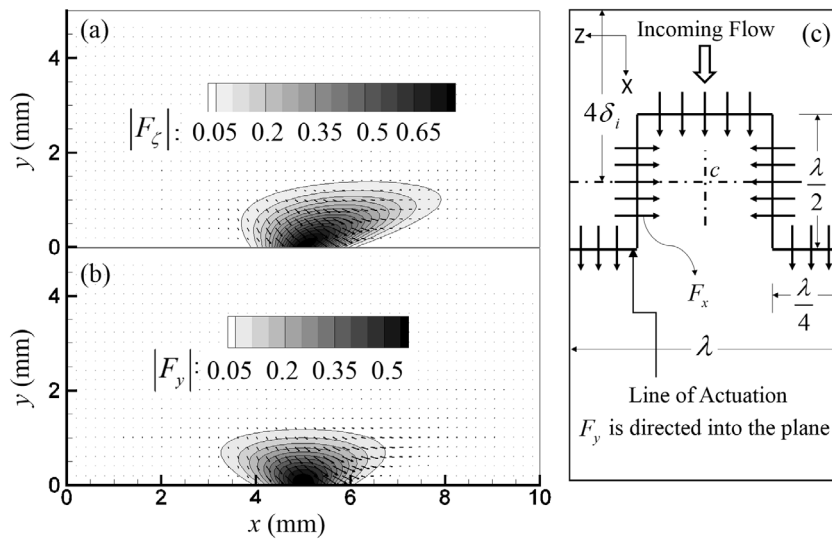


**Figure 3.** Actuator body force along (a) streamwise and (b) wall normal direction with force vectors. (c) Actuator geometry details and forcing directions along the line of actuation.

and their growth in both space and time has also been investigated. Since the actuation follows a serpentine geometry [1, 40, 41] knowledge of the transition mechanism can provide practical understanding of the geometric influence of actuation as a controlled tripping mechanism.

This paper is structured as follows. Section 2 gives the computational approach used for the problems studied, section 3 reports results for and discussion on the ZPGTBL using two kinds of tripping mechanisms and finally conclusions are drawn in section 4.

## 2. Computational approach

As mentioned earlier, the two types of study performed here are transition to turbulence using bypass mechanism and transition using 3D actuation. From here on, the former will be called as case I and the latter as case II. For case I and case II the Reynolds number based on plate length,  $Re_x$  ranges from  $2.5 \times 10^5$  to  $6.25 \times 10^5$  and  $3.75 \times 10^5$  to  $8 \times 10^5$ ,

respectively. For case I,  $Re_\theta$  ranges from 330 to 1250 and for case II it is from 400 to 1100.

### 2.1. Mesh details

The different mesh sizes used for case I and case II have been tabulated in table 1. The streamwise ( $x$ -direction), wall normal ( $y$ -direction) and spanwise ( $z$ -direction) domain sizes, ( $L_x^+$ ,  $L_y^+$  and  $L_z^+$  respectively) are based on the inlet wall unit ( $\Delta y_i^+ = \Delta y_i u_{\tau,i} / \nu$ ) where  $u_{\tau,i}$  is the friction velocity at the inlet and  $\nu$  is the kinematic viscosity, which is held constant for all the mesh sizes. Although, the number of elements ( $N_y$ ) in the wall normal direction is changed,  $\Delta y_i^+$  does not change since more elements are packed in the log layer and the mesh is wall resolved. The number of grid points in the boundary layer ranges over the domain from 40 at the inlet to 44 at the outlet for the coarse mesh, 50 to 60 for the medium mesh, 80 to 90 for the fine mesh of case I and 40 to 44 for case II. The mesh is stretched [42] in the wall normal direction using

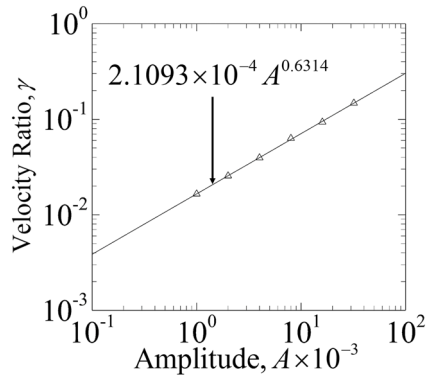


**Figure 4.** Effect on velocity ratio based on different forcing amplitudes for a linear actuator.

$$y(j) = L_y \frac{C\eta}{1 + C - \eta}, \quad \eta = \frac{j-1}{N_y-1}. \quad (1)$$

In equation (1), is the height of the domain in wall normal direction and  $j$  is the grid point. The choice of constant  $C$  gives  $\Delta y_i^+ = 0.9$ . The mesh is uniform in  $x$  and  $z$  directions. However, near the streamwise and wall normal outflow boundaries, the mesh is geometrically expanded and the outlet velocities are relaminarized to Blasius profile using a sink term, similar to a sponge region [43, 44], to avoid any reflections. It should be noted that the mesh parameters chosen here correspond to the grid requirements for wall resolved LES provided by Choi and Moin [45]. The mesh details for case II was chosen based on the mesh study for case I, and was found to be adequate to obtain the relevant turbulent statistics and structures.

## 2.2. Boundary and initial conditions

The Mach number for all the cases studied in this paper is set to 0.5, which is weakly compressible. For case I, the inlet freestream conditions are applied with static pressure ( $P_\infty$ ) of 10132.5 Pa and static temperature ( $T_\infty$ ) of 273 K. The freestream velocity ( $U_\infty$ ) is 165.61 m s<sup>-1</sup>, and the dynamic viscosity ( $\mu_\infty$ ) based on Sutherland's law is  $1.716 \times 10^{-5}$  Ns m<sup>-2</sup>. A Blasius profile corresponding to  $Re_x = 2.5 \times 10^5$ , is used for the streamwise and wall normal velocity at the inlet. Based on this the incoming  $Re_\theta$  is 330. The wall is kept at no slip adiabatic conditions. Both top and outlet boundary conditions are obtained by linear extrapolation with the pressure kept at  $P_\infty$ . Same conditions are used for case II except that  $Re_x = 3.75 \times 10^5$  and  $Re_\theta$  is 400 at the inlet. The density variations are below 2.5% and Van Direct transformations [46] had no impact on the mean and fluctuating components. Blasius profile is also used to initialize all the cases. For case I, the flow is tripped at a location,  $4\delta_i$  (inlet boundary layer thickness for  $0.99U_\infty$ ) from the inlet and the tripping method is similar to the approach taken by Schlatter and Orlu [22] for their baseline case. Next section describes the tripping mechanism for case II.

## 2.3. Actuator forcing mechanism

The SDBD plasma actuators are constructed using two asymmetrically placed electrodes separated using a dielectric

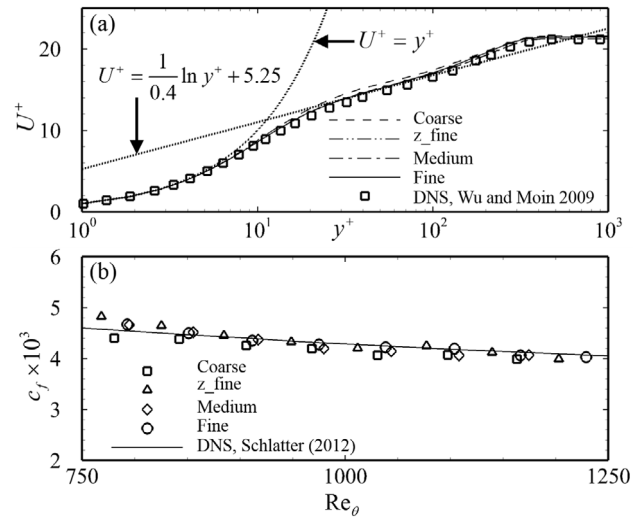


**Figure 5.** Mesh convergence for (a)  $U^+$  at  $Re_\theta = 900$  compared to Wu and Moin DNS data [54]. (b) Skin friction comparison with data fit to different DNS data by Schlatter and Orlu [22].

material. A high voltage (~kV) alternating current is applied to the electrodes across the dielectric material. Radio frequencies are generally used for the applied voltage. One of the electrode is exposed to the surrounding air while the other is encapsulated. A simple depiction of the actuator geometry and operation is shown in figure 1. When high voltage is applied across the electrodes the gas surrounding the exposed electrode ionizes and creates electrons, positive ions and negative ions. Due to the asymmetrically placed electrodes, the electric field directs the ions in its direction which in turn impacts the neutral gas molecules and creates a wall jet flow. Figure 1(b) depicts different actuator geometries obtained by changing the shape of the line of actuation. Figure 1(c) depicts the plasma formed around the exposed electrode for an actuator operating at 14 kV<sub>pp</sub> and 1 kHz. These actuators were made using copper electrodes with 1.5 mm PMMA dielectric. Experimental investigation of serpentine plasma actuators [1, 40] have shown that they create 3D streamwise oriented vortices and the flow moves in a corkscrew path. The fluid is pushed forward and away from the surface. A depiction of the streamwise oriented bound vortical structures generated by a square serpentine actuator at 14 kV<sub>pp</sub> and 10 kHz are shown in figure 2.

The focus here would be on using a body force approximation based on first principles model for simulating square serpentine SBDB actuators. The concept of this forcing mechanism comes from the SDBD plasma actuators which has been used as a flow control device for a variety of applications including airfoil separation control [47], bluff body noise control [48], flow control in cavity flow [34] etc. Different types of body force models were investigated [49] and found to have minor differences in the flowfield near the plasma region. The approach here is to use a body force model formulated by Singh and Roy [50] to simulate the effect of plasma actuators. The geometry of the actuator, corresponds to the class of serpentine plasma actuators introduced by Wang and Roy [40]. The body force distribution [41] for the actuator used in the current study is depicted in figure 3 and is obtained using

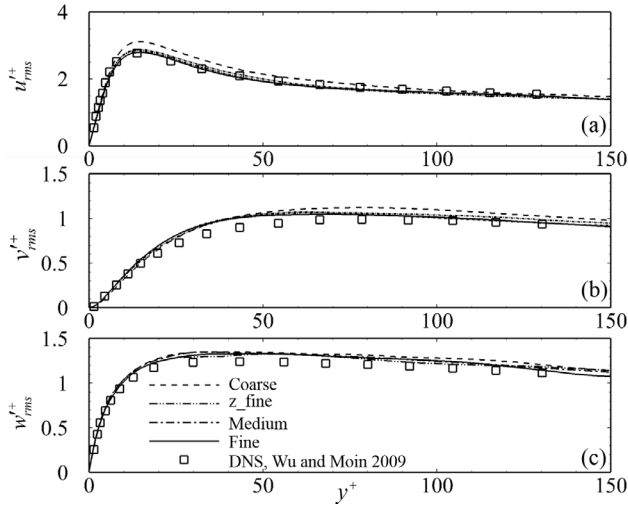


**Figure 6.** Mesh convergence for Reynolds stresses scaled with inner wall coordinates at  $Re_\theta = 900$  compared to DNS data [54]. (a) Streamwise, (b) wall normal and (c) spanwise rms fluctuations.

$$F_\zeta = \frac{F_{\zeta_0}}{\sqrt{F_{\zeta_0}^2 + F_{y_0}^2}} \exp \left\{ - \left[ \frac{(\zeta - \zeta_0) - (y - y_0)}{y - y_0 + y_b} \right]^2 - \beta_\zeta (y - y_0)^2 \right\}$$

$$F_y = \frac{F_{y_0}}{\sqrt{F_{\zeta_0}^2 + F_{y_0}^2}} \exp \left\{ - \left[ \frac{(\zeta - \zeta_0)}{y - y_0 + y_b} \right]^2 - \beta_y (y - y_0)^2 \right\}. \quad (2)$$

In equation (2)  $F_{\zeta_0} = 2.6$ ,  $F_{y_0} = 2.0$ ,  $\beta_\zeta = 1.44 \times 10^6$ ,  $\beta_y = 1.8 \times 10^6$  and  $y_b = 6.65 \times 10^{-4}$ . The last three parameters which provide the extent of the exponential distribution as shown in figures 3(a) and (b). These parameters are scaled such that the body force decays by 99% within  $\delta_i/4$  where  $\delta_i$  is the inlet boundary layer thickness. The location of the actuation is given by  $\zeta_0$  and  $y_0$  which correspond to the points along the line of actuation depicted in figure 3(c). The body force terms are applied such that  $F_y$  is always directed in negative wall normal direction and due to the 2D nature for the serpentine actuators,  $F_\zeta$  is decomposed into two components, namely the streamwise,  $F_x$  and spanwise,  $F_z$  component. The actuator center location given by  $c$  as depicted in figure 3(c) is at a distance  $4\delta_i$  from the inlet. The actuator design shown in figure 3(c) is similar to a square serpentine actuator [1] and its dimensions are given by its wavelength,  $\lambda$  which is equal to the spanwise length of the domain.

The forcing terms are modulated with a sinusoidal frequency,  $\omega$  of 1 kHz, typical for a SDBD actuator, and an amplitude  $A$  given by

$$F_{b_\zeta} = AF_\zeta |\sin(\omega t)|$$

$$F_{b_y} = AF_y |\sin(\omega t)|. \quad (3)$$

Both  $F_{b_\zeta}$  and  $F_{b_y}$  are implemented as body force terms in the momentum and energy equations of Navier Stokes equations. The amplitude  $A$  was determined by conducting simulations of the actuator in quiescent conditions for different values of  $A$ , to obtain the maximum mean velocity magnitude generated,  $u_p$  and consequently the ratio,  $\gamma = u_p/U_\infty$ . For the present study,  $\gamma$  is chosen to be 0.1. It should be noted that the velocity induced by this forcing is around  $16.5 \text{ m s}^{-1}$ , while the current state of the art actuators can generate utmost

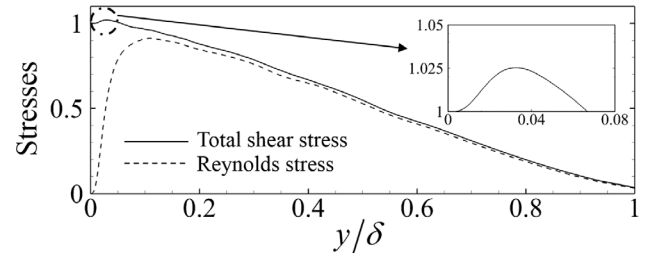


**Figure 7.** Variation of total shear stress and Reynolds shear stress with outer coordinates at  $Re_\theta = 1030$ .

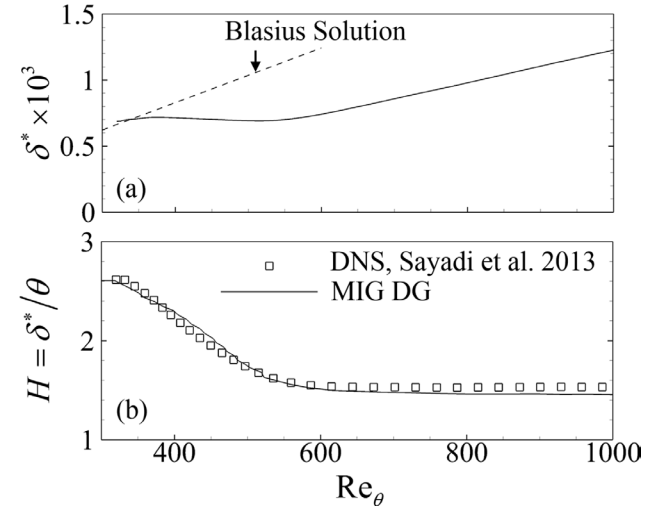


**Figure 8.** (a) Variation of displacement thickness  $\delta^*$  with  $Re_\theta$ . (b) Shape factor profile showing transition from laminar to turbulent flow.

$11 \text{ m s}^{-1}$  [51]. However, the important parameter is the velocity ratio, which has been discussed in section 3.3. The parameters chosen can be related to a square serpentine actuator with a ground electrode width of 3.125 mm operating at 1 kHz and 25 kV<sub>pp</sub>. These numbers are obtained using extrapolation of results by Singh and Roy [50] and does not consider effects of thrust saturation [52] in plasma actuators. The relationship between  $A$  and  $\gamma$  is depicted in figure 4. To avoid symmetry in the spanwise direction, an additional normally distributed random perturbation of amplitude 0.1A, was added to the amplitude  $A$ . Since an absolute value of the sine wave is used, the forcing occurs at a frequency  $2\omega$ , which gives a Strouhal number,  $St = 2\omega\delta_i/U_\infty = 0.584$  ( $\omega$  is in  $\text{rad s}^{-1}$ ) and a non-dimensional frequency of  $f \times 10^6 = 2\omega\nu/U_\infty^2 \approx 60$ .

#### 2.4. Numerical details

The unfiltered compressible Navier Stokes equations without incorporating any turbulence modelling, was used to simulate the turbulent flow. The simulations were carried out using modal discontinuous Galerkin method implemented in our in-house Multiscale Ionized Gas (MIG) flow code. The solutions inside the discontinuous elements were interpolated using Legendre polynomials. The spatial discretization was done using a third order accurate scheme ( $P = 2$ ) and two step fully explicit Runge Kutta method is used for the temporal terms. The numerical integration employed uses Gauss–Legendre

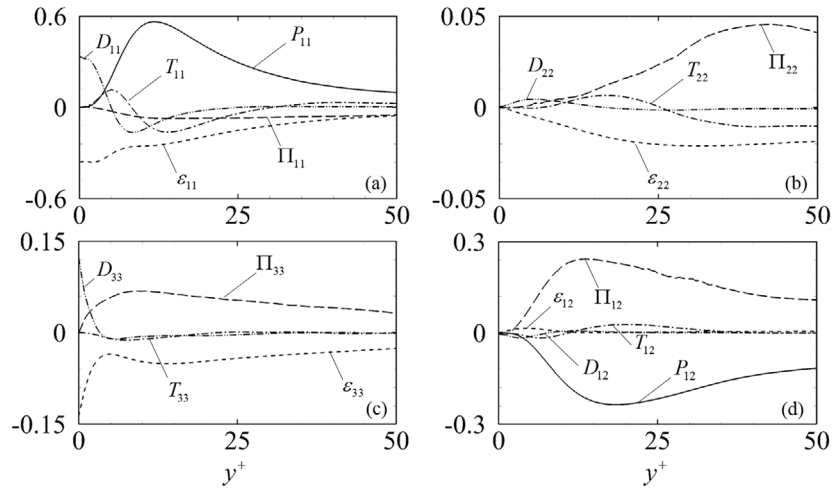


**Figure 9.** Variation of Reynolds stress budget terms with inner wall coordinates at  $Re_\theta = 900$ . (a)  $u'^2$ , (b)  $v'^2$ , (c)  $w'^2$  and (d)  $u'v'$ . All the terms are scaled using inner wall parameters.

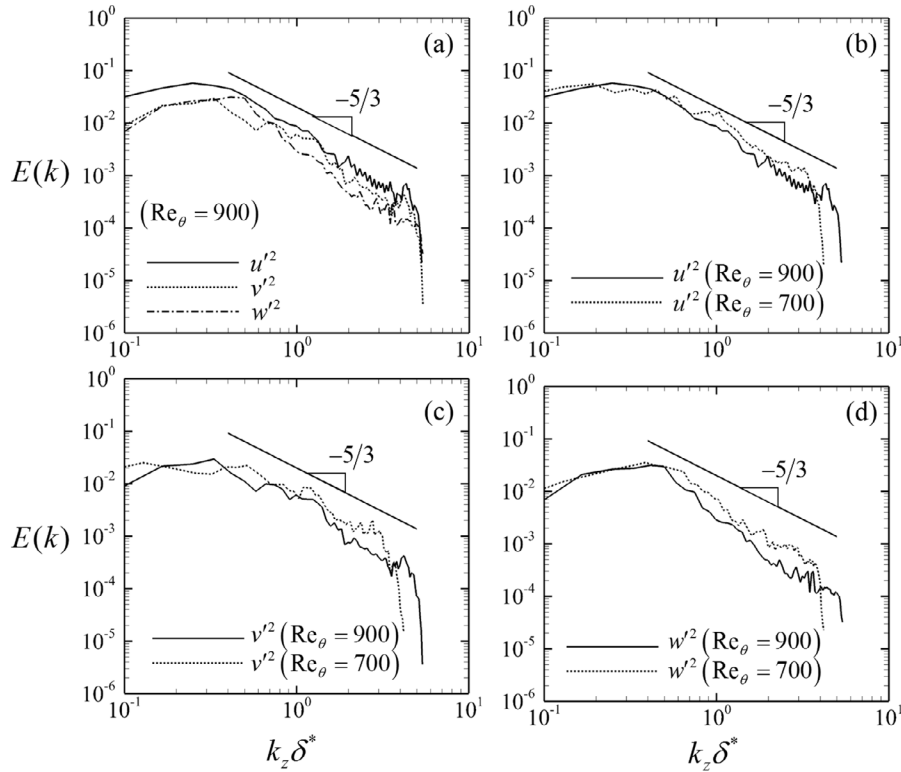


**Figure 10.** Energy spectrum of fluctuating components in the spanwise direction at  $y/\delta^* = 1$ . (a) Spectrum at  $Re_\theta = 900$ . Comparison of spectrum at  $Re_\theta = 700$  and  $900$  for (b) streamwise, (c) wall normal and (d) spanwise fluctuations.

quadrature rules with  $P + 3$  integration points in each direction. The local Lax–Friedrichs flux was used for the convective numerical flux since it gives similar results to other numerical fluxes [27, 30, 53] for the current order approximation and local discontinuous Galerkin method was used for the viscous numerical fluxes. For all the cases, the non-dimensional time step is  $\Delta t^+ = u_{\tau,i}^2 \Delta t / \nu = 0.0048$ . The flow was allowed to convect two times over the entire streamwise length at a convective speed of around  $0.75U_\infty$ , before the mean flow calculations were started. This corresponds to about  $3100\nu/u_{\tau,i}^2$  and the mean flow calculations were carried out over a period of  $1600\nu/u_{\tau,i}^2$ .

### 3. Results

#### 3.1. Turbulent statistics for case I

For case I the mesh sizes tested showed that the wall scaled mean velocity,  $U^+ = \bar{U}/u_\tau$ , where  $\bar{U}$  is the time and spanwise averaged solution, has minor variations due to mesh size as depicted in figure 5(a). The results slightly over predict the solution in buffer and log layer region when compared to the DNS results [54]. However, the viscous sublayer is accurately captured. The slope of log layer is found to be 0.4 and the constant as 5.25. The skin friction,  $c_f$  in figure 5(b) shows

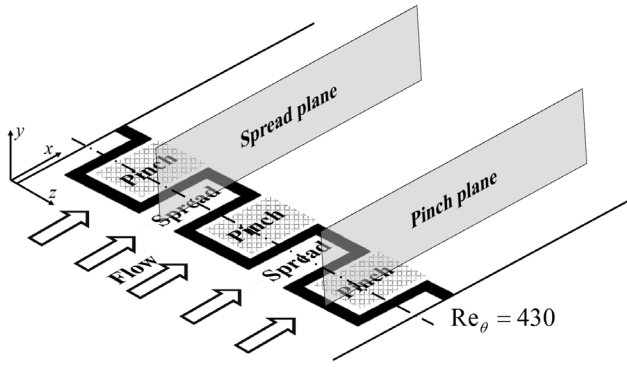


**Figure 11.** Schematic of the actuation pinch plane and spread plane.

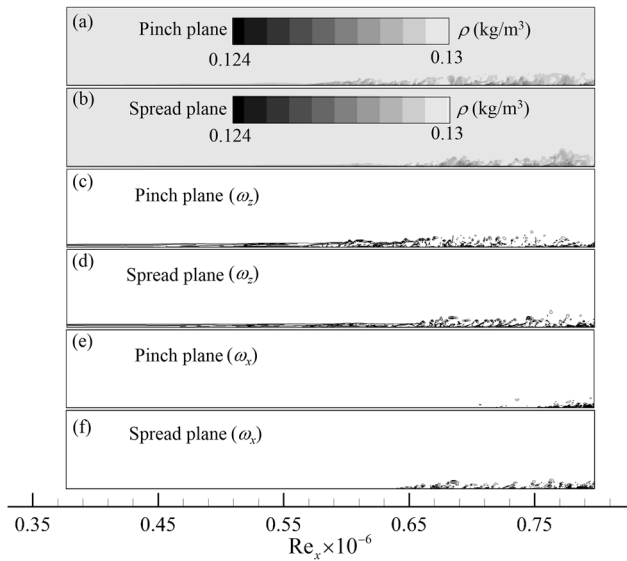


**Figure 12.** Instantaneous contours of different flow parameters in the pinch plane and spread plane. Contours of (a) and (b) density, (c) and (d) spanwise vorticity and (e) and (f) streamwise vorticity. There are 11 contour lines equally spaced between  $-5 \times 10^4$  to  $5 \times 10^4 \text{ s}^{-1}$  in figures (c)–(f).

good agreement with published DNS data [22] for all the mesh sizes.

The normalized root mean square (rms) streamwise fluctuating velocity,  $u'_{rms}^+ = \sqrt{u'^2}/u_\tau^+$  depicted in figure 6, shows that the coarse mesh is not suitable to resolve the perturbations. Doubling the mesh density in the spanwise direction solves this issue. The Reynolds stresses match with the DNS results [54] with an rms error of about 5% corresponding to wall normal fluctuations. The peak value for  $u'_{rms}^+$  is 2.82 and it occurs at  $y^+ = 14$  ( $y/\delta = 0.04$ ) for  $Re_\theta = 900$  for the fine mesh. The wall normal and spanwise fluctuations have peak values of 1.09 and 1.33 respectively. The differences in rms fluctuations when compared to DNS data are fairly insignificant since similar variations in fluctuating components have not only been seen experimentally but also numerically at similar Reynolds numbers. Factors such as spatial resolution of probes, measuring apparatus, tripping mechanism etc

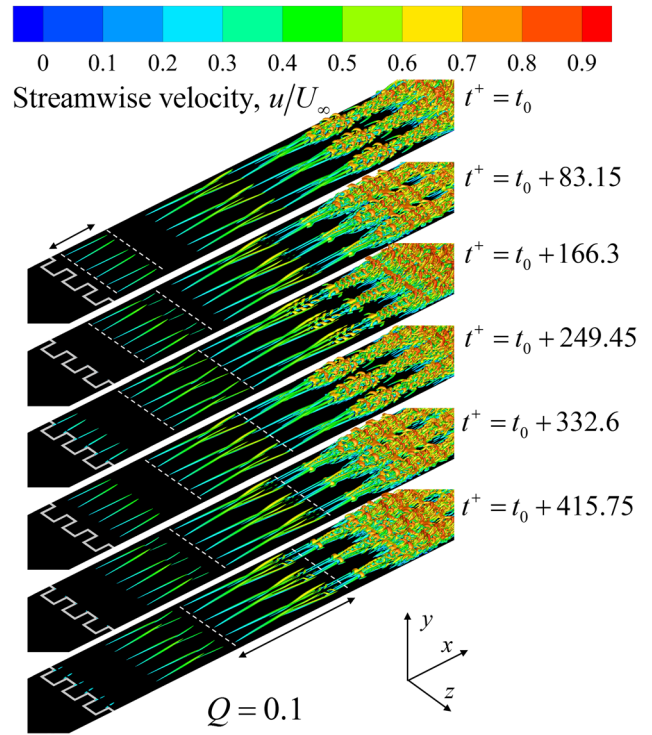


**Figure 13.** Instantaneous normalized  $Q$  criterion iso-surfaces ( $Q = 0.1$ ) shown at different instances in time depicting the growth of turbulent structures. Domain is duplicated three times for better visualization.

can affect the experimental data while grid resolution, inflow length, tripping method, domain size etc can impact the numerical data [55]. Therefore, the mesh sizes equal or more than the  $z_{fine}$  case is adequate to resolve the fluctuations. The medium mesh case is used for rest of the visualizations and comparisons of case I. However, it should be noted that for the present study higher than second order moments were not compared, as suggested by Spalart [10].

In figure 7 the total shear stress  $\tau^+ = (\nu \partial \bar{U} / \partial y)^+ - \overline{u'v'}^+$ , is plotted against outer coordinates at  $Re_\theta = 1030$ . Similar to Wu and Moin [54], the data shows that the maximum shear stress does not occur at the wall, but at around  $y/\delta = 0.03$  or  $y^+ = 12$  (see inlay). This is the same location where  $u'_{rms}^+$  is maximum. This behavior is observed throughout the turbulent boundary layer ranging from  $Re_\theta = 670$  to 1030. This has not been seen by other authors [10, 22] and also for channel flow cases where the stress is linear.

The integral quantities shown in figure 8, depict the variation of displacement thickness  $\delta^*$  and the shape factor  $H$  with  $Re_\theta$ . Both displacement thickness and shape factor shows the deviation from the Blasius laminar solution to the turbulent solution. The shape factor shown in figure 8(b) is in good agreement with the DNS results of Sayadi *et al* [56] for K-type transition.

In figure 9 the Reynolds stress budget terms are plotted at  $Re_\theta = 900$  near the wall. The equations to determine these parameters are given below [57]

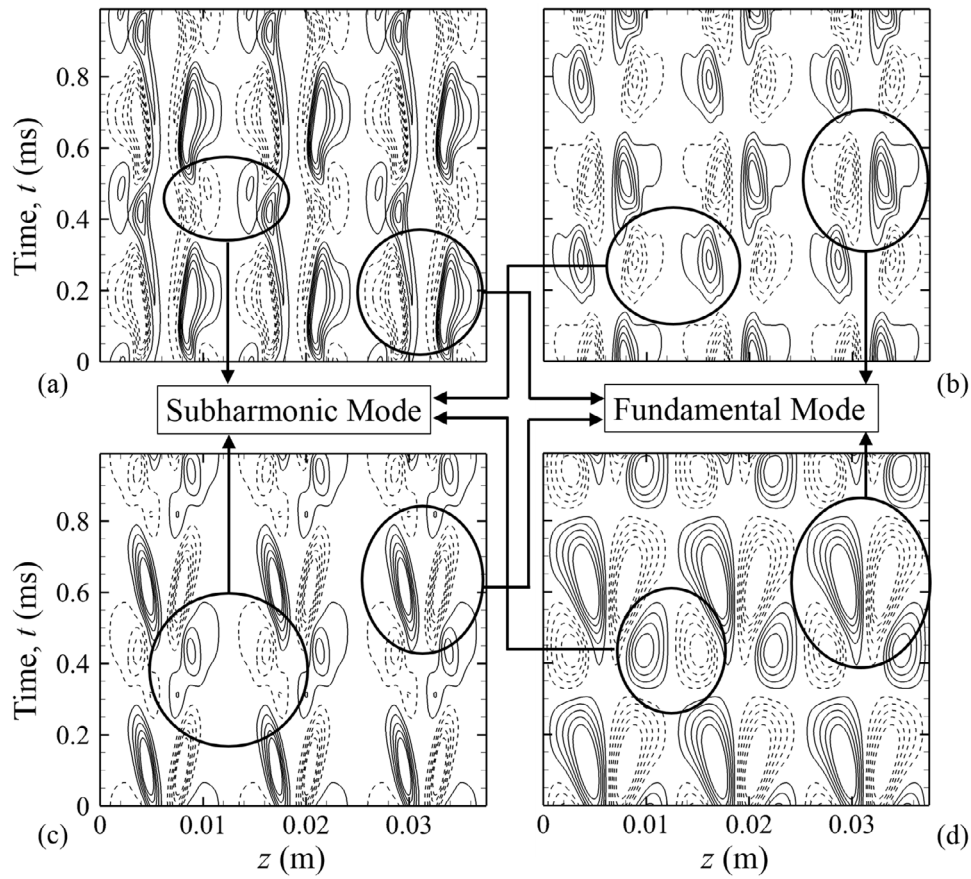


Figure 14. Variations of instantaneous spanwise fluctuations over time depicting staggered pattern of oblique wave transition at  $Re_\theta = 500$  for (a)  $y^+ = 10$ , (b)  $y^+ = 30$ , (c)  $y^+ = 50$  and (d)  $y^+ = 100$ .

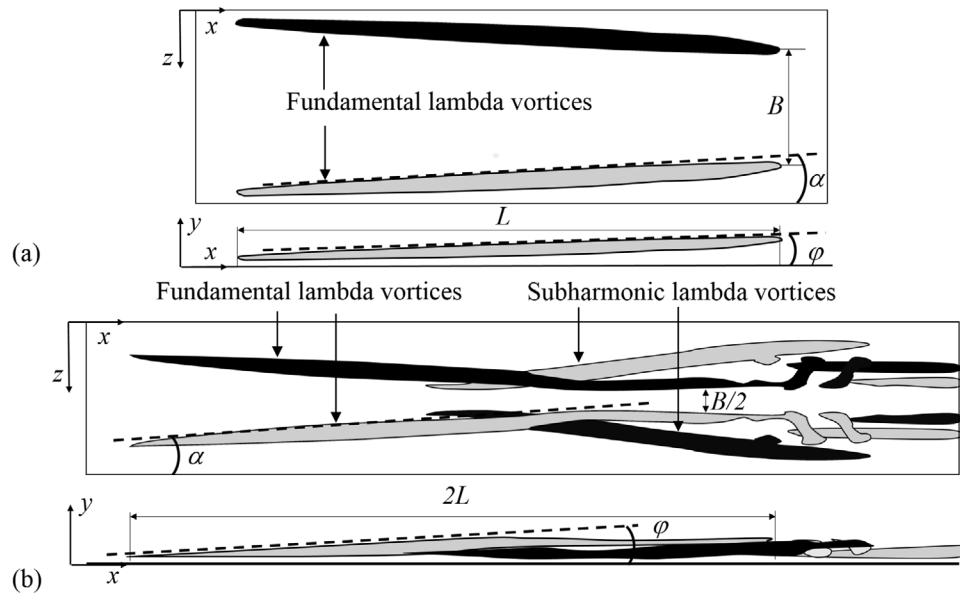


Figure 15. Approximate representation of vortical structures at (a)  $t^+ = t_0$  and (b)  $t^+ = t_0 + 415.75$ . The shaded grey structures have clockwise rotation and the shaded black structures have anticlockwise rotation.

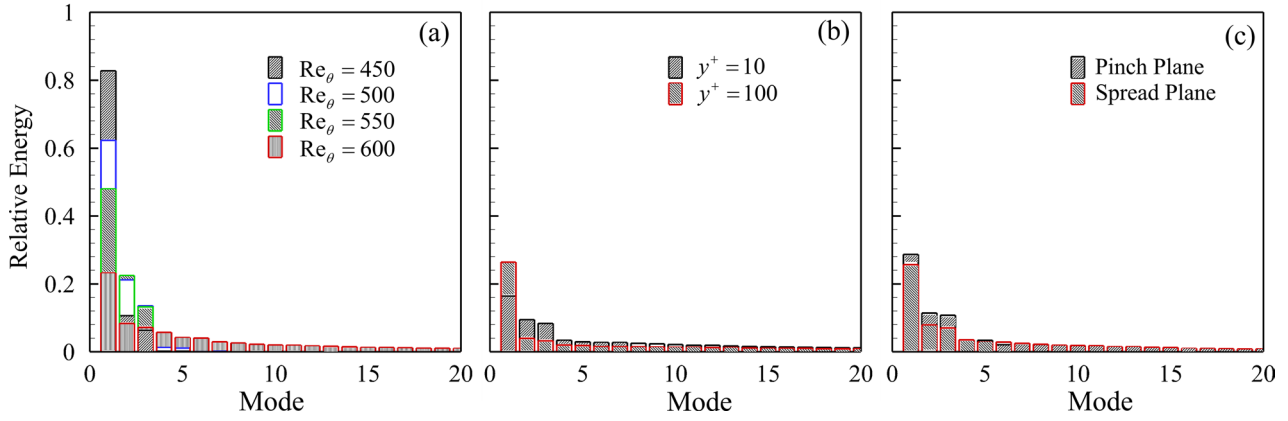


Figure 16. Relative energy content for different modes at different (a)  $Re_\theta$  locations, (b)  $y^+$  planes and (c) pinch and spread planes.

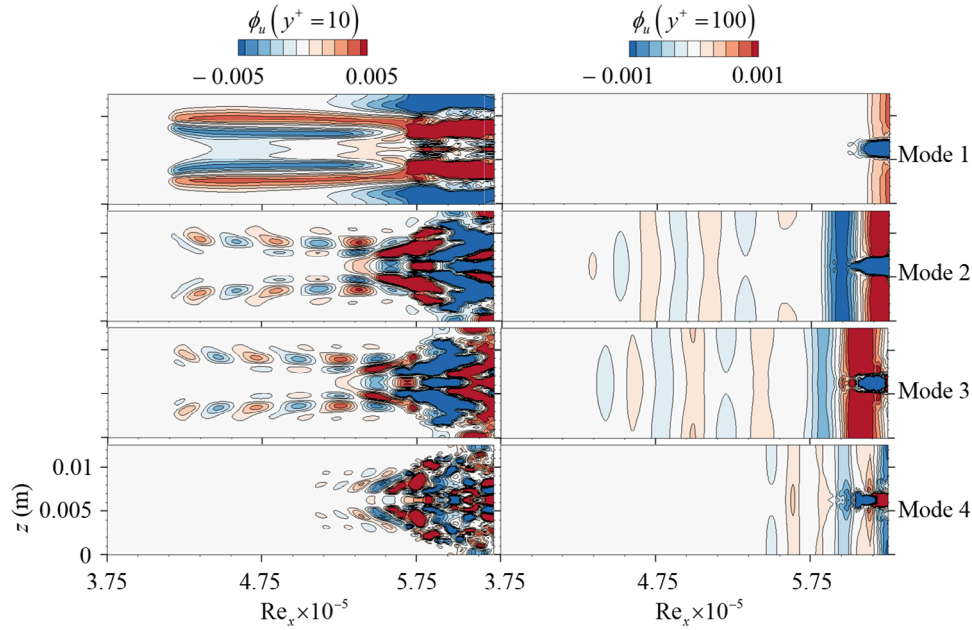


Figure 17. Relative energy content for different streamwise modes along two  $y$ -planes.

$$\begin{aligned}
 P_{ij} &= - \left( \overline{u'_i u'_k} \overline{U}_{j,k} + \overline{u'_j u'_k} \overline{U}_{i,k} \right) \nu / u_\tau^4, & \text{Production rate} \\
 \varepsilon_{ij} &= -2 \left( \overline{u'_i u'_j u'_k} \right) \nu^2 / u_\tau^4, & \text{Dissipation rate} \\
 T_{ij} &= - \left( \overline{u'_i u'_j u'_k} \right) \nu / u_\tau^4, & \text{Turbulent transport rate} \\
 D_{ij} &= \left( \overline{u'_i u'_j} \right)_{kk} \nu^2 / u_\tau^4, & \text{Viscous diffusion rate} \\
 \Pi_{ij} &= - \left( \overline{u'_i p'_j} + \overline{u'_j p'_i} \right) \nu / \rho u_\tau^4, & \text{Velocity pressure-gradient term.}
 \end{aligned}
 \tag{4}$$

The subscripts  $i, j$  and  $k$  to  $u'$  in equation (4) correspond to the streamwise, wall normal and spanwise fluctuating velocity. All the terms are scaled using wall parameters. The budget terms show that the Reynolds stresses are predominant in the  $u'^2$  and  $u'v'$  components. The terms also balance out showing that the mean flow quantities have reached steady state. These results show similar behavior and trends when compared to the data by Spalart [10].

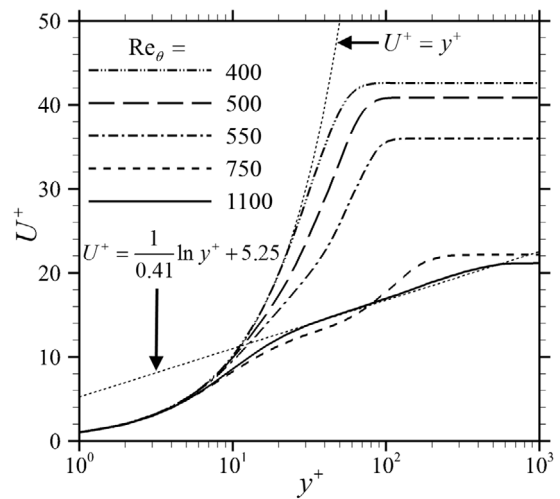
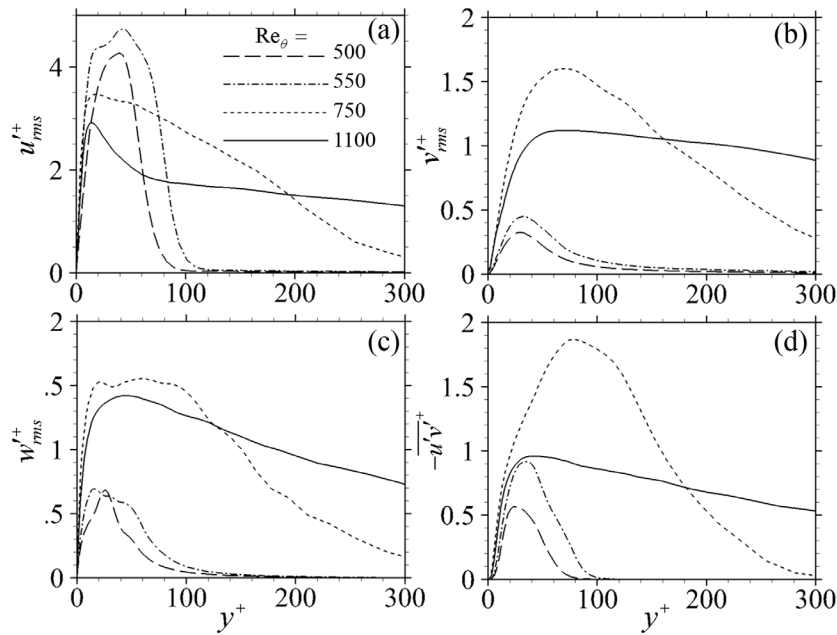


Figure 18. Time and span averaged mean velocity profile variation with inner coordinates scaled with wall parameters at different  $Re_\theta$ .



**Figure 19.** Wall scaled variation of (a) streamwise, (b) wall normal, (c) spanwise and (d)  $-\overline{u'v'}$  variation with inner wall coordinates.

The energy spectrum is plotted in figure 10 for the instantaneous fluctuating velocity components at  $y/\delta^* = 1$ . It can be seen that the energy levels in the inertial region for all the perturbations are similar which indicates the flow is isotropic in nature. There is a minor decrease in energy as the  $Re_\theta$  increases from 700 to 900. It can also be seen that as the Reynolds number is increased the wavenumbers grow higher due to the reduction in eddy size. For all the figures,  $-5/3$  slope line is also shown for reference.

### 3.2. Instantaneous flowfield for case II

The 3D forcing due to the actuator creates two kinds of regions, namely the pinching region (center  $z$ -plane), where the forces are directed towards each other and the spreading region (spanwise boundary planes) where the forces are directed away from each other. The direction of forces is depicted in figure 3(c). For reference, figure 11 gives a depiction of the pinch plane and the spread plane of the actuator. It should be noted that only one wavelength of the actuator is simulated and the results are shown with the domain duplicated three times.

The flow appears to turbulize faster downstream of the pinch region compared to the spread region as shown in the density contours in figures 12(a) and (b) but the variations in density for each plane is negligible. Similar behavior can be observed for spanwise oriented vortices ( $\omega_z$ ) in figures 12(c) and (d). However, for streamwise oriented vortices ( $\omega_x$ ) the transition occurs earlier in the spread plane compared to the pinch plane as shown in figures 12(e) and (f).

To investigate the vortical structures generated by the actuation,  $Q$  criterion iso-surface ( $Q = 0.1$ ) is plotted in figure 13. It shows the time evolution of the quasi streamwise oriented vortices generated by the actuator into 3D structures. The lambda shaped vortices interact with the structures

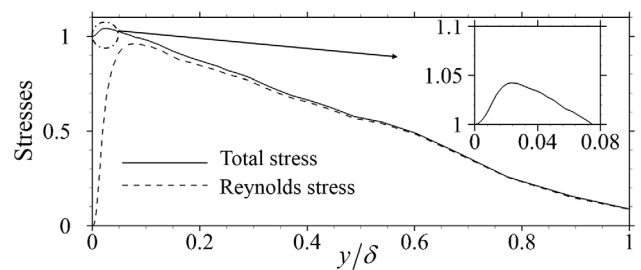


**Figure 20.** Variation of wall scaled total shear stress and Reynolds stress,  $-\overline{u'v'}$  with outer coordinates at  $Re_\theta = 1100$ .

downstream as well as upstream to create a staggered set of harmonic and subharmonic lambda vortices similar to an oblique wave transition. These have been experimentally and numerically tested using speakers and ribbons [58, 59] and with a pair of oblique waves [60, 61]. Although the frequency of actuation is kept at  $St = 0.584$ , the transition occurs through the subharmonic mode which involves a fundamental mode and a subharmonic mode with a frequency half of the fundamental mode. The lambda structures are lifted from the plate due to which their tail end moves slower compared to the front, and consequently they grow in time. The growth is shown by the increase in spacing between the dashed white lines. Since a periodic sine wave forcing is used, similar structures are generated every  $t^+ = 241.12$  which is equivalent to the time period of  $1/2\omega$  (here  $\omega$  is the forcing frequency of the actuation in hertz).

In figure 14 two-time periods, based on the time period  $T = 1/2\omega$  of the actuator are plotted for the spanwise fluctuations at different  $y^+$  locations for  $Re_\theta = 500$ . The spanwise domain is duplicated three times. The flow is from top to bottom since the  $y$ -axis is time. The dashed lines are negative fluctuations and solid lines are positive fluctuations. As the structures grow in time they form staggered patterns of

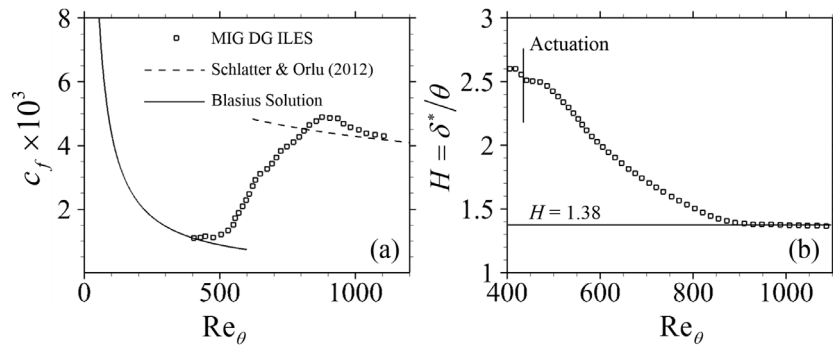


Figure 21. Variation of (a) skin friction and (b) shape factor with  $Re_\theta$ .

positive and negative spanwise fluctuations. The subharmonic mode has a different structure compared to the fundamental mode and appears in between the two fundamental modes.

This behavior of two modes is unlike most of the controlled forcing functions which requires the input of a fundamental and a subharmonic frequency [56, 62] or an oblique wave [58, 63]. For supersonic flat plate boundary layer, the most unstable mode is oblique so suction and blowing [64] can create this type of transition. Also, to confirm whether the combined effect of pinching and spreading created this type of transition, horseshoe geometry was simulated (results not shown here) and similar type of transition was obtained. Therefore, the serpentine geometry forcing does not need to operate on different frequencies to achieve the oblique transition and the pinching effect is the major contributor of this type of transition. Also, the oblique transition is known to transition faster compared to the standard secondary instability mechanism with similar disturbance amplitude [63]. When infinitesimal 2D disturbances are added to the flow, it first goes through the linear instability region and then secondary instability region. The initial amplitudes required for the secondary instability are almost two orders of magnitude higher than that required by oblique mode breakdown [65]. Therefore, we conclude that a single serpentine line of actuation for the geometry considered, can enhance transition for similar initial perturbation when compared to other secondary instability scenarios, due to formation of oblique modes.

To study the structures in more detail two instances in time are picked from figure 13, that is at  $t^+ = t_0$  and  $t^+ = t_0 + 415.75$ . Figure 15 depicts these structures. The lift angle on the  $x$ - $y$  plane of the structure is denoted as  $\varphi$  and the polar angle on the  $x$ - $z$  plane is  $\alpha$ . The length of the structure is given by  $L$  and the spacing between the front ends is  $B$ . It should be noted that the structures in black have anticlockwise rotation while the structures in grey have clockwise rotation. If figures 15(a) and (b) are compared, it can be seen that  $\varphi$  and  $\alpha$  barely change while  $L$  grows to  $2L$  and  $B$  reduces to  $B/2$ . The development of these vortices is dependent mainly on the proximity of the front end of the lambda structures and the distance from the upstream lambda vortices of the fundamental harmonic mode. Unlike the fundamental harmonic lambda vortices, the subharmonic vortices generated, are not inclined and their growth is attributed to the growth in strength of their interaction with the upstream fundamental mode. The

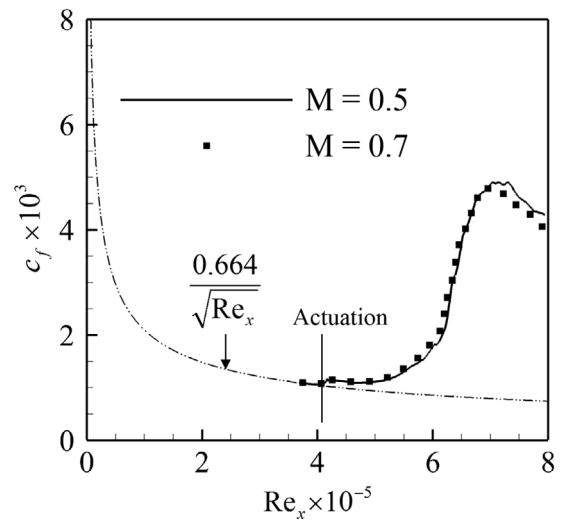
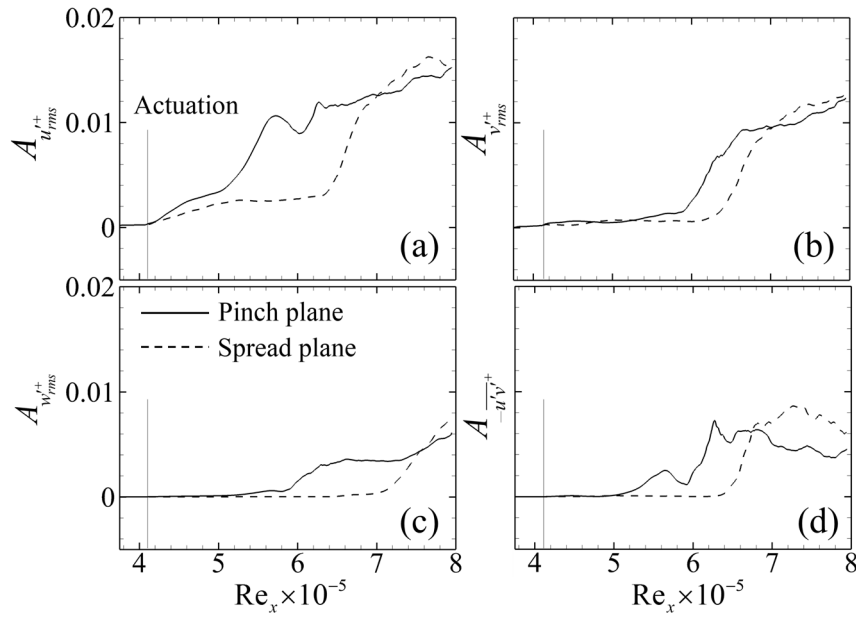


Figure 22. Comparison of skin friction for different Mach numbers at  $\gamma = 0.10$ .

lambda structures start breaking down once the pair of purely spanwise oriented vortices start to develop at the two front ends. The pair of spanwise oriented vortices coalesce together and turn into hairpin vortices, to generate fully turbulent flow.

Since the actuator creates different modes a proper orthogonal decomposition (POD) on the velocity flowfield is conducted to look at the most energetic modes and the coherent structures in the spanwise direction. The POD method was first proposed by Lumley [66] to study turbulent structures and an in-depth analysis and procedure can be found in Berkooz *et al* [67]. The snapshot method proposed by Sirovich [68] is used here. Data from different planes in  $x$ -,  $y$ - and  $z$ -directions are recorded. A total of equally spaced  $N = 132$  snapshots were chosen over a time period of  $T = 3/2\omega$ . Figure 16 shows the relative energy content for first 20 modes at different locations in the transitional region. At  $Re_\theta \leq 550$  most of the energy is in the first three modes. There is some energy in the fourth and fifth mode at  $Re_\theta = 500$  which is not present at  $Re_\theta = 550$ . In the  $y^+$  planes, the energy content in the dominant mode is below 20% and the second and third dominant modes also have similar as well as significant energy in comparison. This can also be seen in the pinch and spread planes. The pinch plane has about 4% more energy content than the spread plane.

The coherent structures are further investigated by looking at the different modes obtained using POD analysis. Figure 17



**Figure 23.** Variation of growth parameter with  $Re_x$  for (a)  $u'_{rms}+$ , (b)  $v'_{rms}+$ , (c)  $w'_{rms}+$  and (d)  $-\overline{u'v'}$ .

shows the streamwise POD modes for two  $y$ -planes. The sub-harmonic mode (mode 2) appears closer to the wall. Away from the wall the mode is 2D in nature with zero spanwise wavenumber. This behavior is seen for higher modes also. Mode 1 has the same spanwise wavenumber in spanwise direction as mode 2 and mode 3, but has but has no streamwise wavenumber unlike the other modes. Mode 2 and mode 3 are similar in behavior and energy content (oblique modes) with a small phase shift in streamwise direction.

### 3.3. Turbulent statistics for case II

The mean flow characteristics are plotted for different  $Re_\theta$  values to depict the transition process from laminar to fully turbulent region in figure 18. At the later stages of transition, the log layer region has a lower velocity compared to the fully turbulent region. The Reynolds stresses depicted in figure 19 show that the peak streamwise fluctuations first increases and then starts decaying till it reaches fully turbulent region.

Similar to case I the peak value of total shear stress shown in figure 20 does not occur at the wall, but at around  $y/\delta = 0.03$  or  $y^+ = 12$  (see inset). The transition occurs over the region  $Re_\theta = 420$  to  $780$  after which the flow becomes fully turbulent. This can be clearly seen in figure 21(a) for the skin friction. Since the forcing is of large magnitude  $\gamma = u_p/U_\infty = 0.1$  the flow quickly transitions to turbulence. The shape factor shown in figure 21(b) has a value of around 1.38 in the fully turbulent region. There is a change in slope of the shape factor at the actuator location as it increases the momentum of the fluid near the wall thus reducing the momentum thickness and increasing the shape factor.

To confirm whether the velocity ratio  $\gamma$  is the important factor in the transition process a similar simulation was performed with  $\gamma = 0.10$  for  $M = 0.7$  with the same non-dimensional parameters and mesh size as the  $M = 0.5$  case

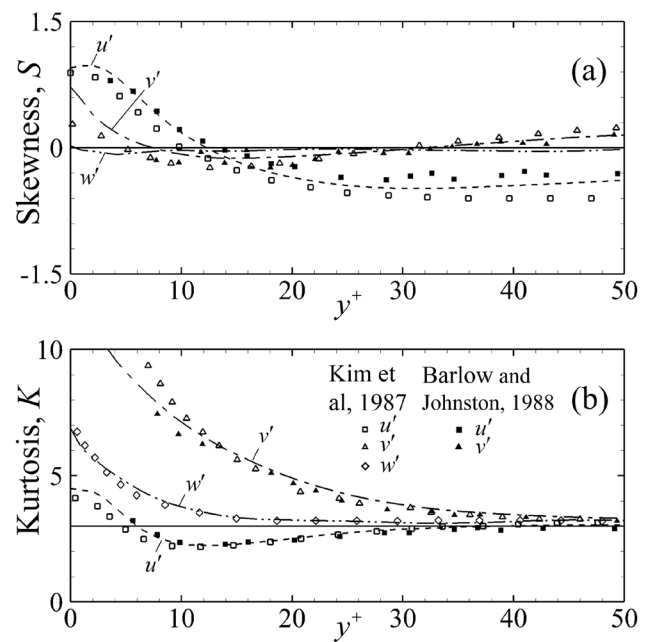


**Figure 24.** Variation of (a) skewness and (b) kurtosis at  $Re_\theta = 1100$  compared with DNS and experimental results.

given in section 2. For this study skin friction is compared for the  $M = 0.5$  and  $M = 0.7$  case in figure 22. It is evident that the flow transitions almost identically for both the cases, with obvious reduction in the fully turbulent skin friction due to increase in Mach number. Identical structures were formed in both the cases. Therefore, it is apparent that the velocity ratio plays an important role in controlling the transition process, independent of these two Mach numbers studied. Similar influence may be expected from state of the art plasma actuators producing velocities up to  $11 \text{ m s}^{-1}$  [51] when used with Mach numbers below 0.3, in comparison to the current velocity of  $16.5 \text{ m s}^{-1}$  used with  $M = 0.5$ .

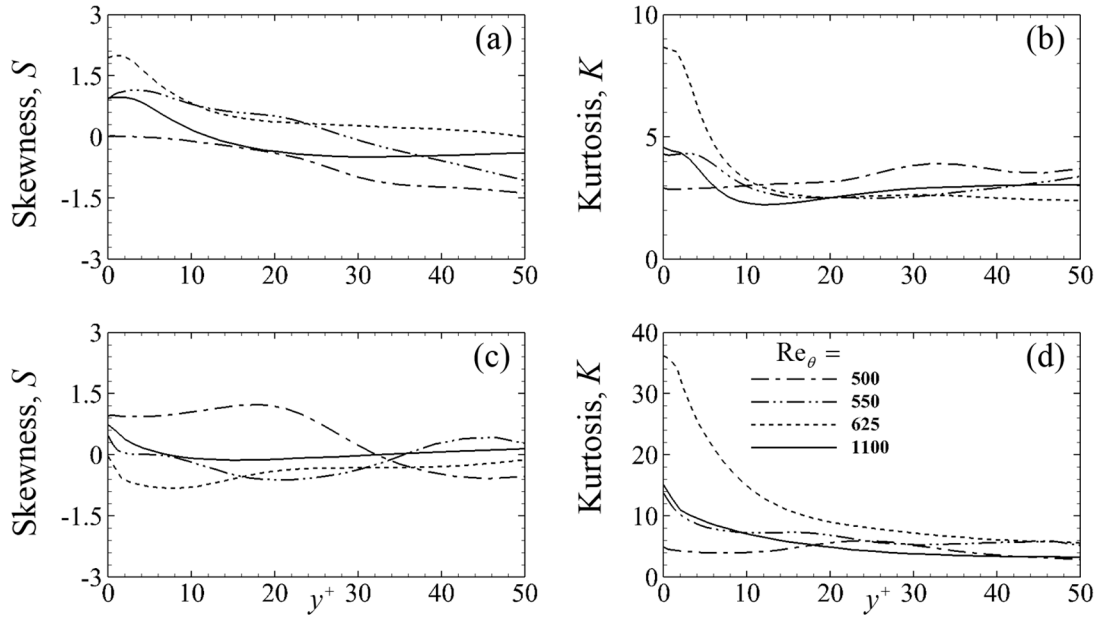


**Figure 25.** Variation of skewness and kurtosis for (a) and (b)  $u'$  and (c) and (d)  $v'$  at different  $Re_\theta$  values.

To investigate the growth of fluctuations a growth parameter  $A_\psi$  is defined as

$$A_\psi = \int_0^{L_y} \psi(x, y, z) dy. \quad (5)$$

In equation (5)  $\psi$  is the variable for which the magnitude is being evaluated, for example wall scaled root mean square streamwise velocity fluctuations  $u'_{rms}^+$ . In figure 23 the growth parameter is plotted for the pinch and spread plane. The spread plane shows the transition to be at  $Re_x \approx 6.5 \times 10^5$  based on the streamwise and wall normal fluctuation growth as well as  $-u'v'^+$  growth parameter. However, the spanwise fluctuations does not transition up to  $Re_x \approx 7 \times 10^5$ . This may be due to the presence of strong streamwise oriented vortices which create perturbations in the streamwise and wall normal directions. The spanwise perturbations on the spread plane occurs when hairpin vortices start forming and interacting with each other in the later stages of transition. From close inspection, this can be observed in the  $-u'v'^+$  growth parameter of the spread plane in figure 23(d) which shows a slope change at  $Re_x \approx 7 \times 10^5$  indicative of the flow crossing the transitional region and reaching turbulence.

The skewness,  $S$  and kurtosis,  $K$  shown in figure 24 are given by

$$S(u') = \frac{\overline{u'^3}}{(\overline{u'^2})^{3/2}}; K(u') = \frac{\overline{u'^4}}{(\overline{u'^2})^2}. \quad (6)$$

Both  $S$  and  $K$  are plotted at  $Re_\theta = 1100$  and compared to experimental data for a flat plate boundary layer by Barlow and Johnston [69] and numerical data for channel flow by Kim, Moin and Moser [70]. The data from experimental results correspond to  $Re_\theta = 1100$ . The results show good agreement with the published data. For reference, the normal distribution values for skewness ( $S = 0$ ) and kurtosis ( $K = 3$ ) are also shown in solid line. The large positive flatness of  $v'$

shows the highly intermittent nature of fluctuations occurring near the wall.

In figure 25 the variation of skewness and flatness is shown at different regions of transition. Closer to the actuation the skewness is negligible near the wall for  $u'$ , but  $v'$  has similar skewness to that of the fully turbulent region. In figure 25(a) a larger skewness near the wall is seen for  $u'$  at the later stages of transition where the breakdown of lambda vortices occurs ( $Re_\theta = 550 - 780$ ) whereas  $v'$  has a larger value around  $Re_\theta = 450 - 550$ . The large intermittency shown in the kurtosis plots takes place at the later stages of transition which drops down to almost half the value in fully turbulent region.

#### 4. Conclusion

Two kinds of analyses for transition to turbulence have been studied. Both mechanisms use nonlinear perturbation to generate turbulent flow. Validation studies for ZPGTBL using Schlatter and Orlu [22] tripping mechanism via bypass transition has been provided. The largest  $Re_\theta$  tested for this case was 1250. Mesh convergence and validation studies shows that wall resolved DG ILES also provide reasonably accurate results. Unlike previous published literature the total shear stress was found to be maximum at  $y/\delta = 0.03$  instead of being at the wall.

Flow transition was also examined using a 3D actuation method similar to the effect of a square serpentine plasma actuator. The perturbation amplitude is 10% ( $\gamma = 0.1$ ) of the freestream velocity and therefore is highly nonlinear. It creates turbulent structures directly via secondary instabilities which follows oblique wave transition and therefore the transition is faster compared to the standard secondary instability mechanism with similar disturbance amplitude. The onset of turbulence due to this type of actuation occurs at an earlier location for the pinch plane when compared to the spread plane of the actuator. The relevant structures such

as lambda vortices, quasi-streamwise vortices, hairpin vortices, etc are studied. The actuation creates low speed streaks which become unstable and breakdown into pairs of hairpin vortices before making the flow fully turbulent. Although the frequency of the controlled actuation is kept at  $St = 0.584$ , the transition occurs through the subharmonic mode (H-type) which involves a fundamental mode and a subharmonic mode with a frequency half of the fundamental mode. This is attributed to the strong interaction between two consecutive lambda vortices. Similar to the bypass transition the total shear stress for the controlled actuation was again found to be the maximum at  $y/\delta = 0.03$ .

## Acknowledgments

This work was partially supported by AFOSR grant FA9550-15-1-0424 monitored by Drs R Ponnappan and Douglas Smith.

## ORCID iDs

Arnob Das Gupta  <https://orcid.org/0000-0002-6978-7791>  
Subrata Roy  <https://orcid.org/0000-0002-2316-0854>

## References

- [1] Durscher R J and Roy S 2012 Three dimensional flow measurements Induced from serpentine plasma actuators in quiescent air *J. Phys. D: Appl. Phys.* **45** 035202
- [2] Klebanoff P S and Diehl Z W 1952 *Some Features of Artificially Thickened Fully Developed Turbulent Boundary Layers with Zero Pressure Gradient* (National Advisory Committee for Aeronautics) pp 1–27 (<https://ntrs.nasa.gov/archive/nasa/casi.ntrs.nasa.gov/19930092145.pdf>)
- [3] Coles D E 1962 *Phys. Fluids* **7** 1403–23
- [4] Kline S J, Reynolds W C, Schraub F A and Runstadler P W 1967 The structure of turbulent boundary layers *J. Fluid Mech.* **30** 741–73
- [5] Murlis J, Tsai H M and Bradshaw P 1982 The structure of turbulent boundary layers at low Reynolds numbers *J. Fluid Mech.* **122** 13–56
- [6] Österlund J M 1999 *Experimental Studies of Zero Pressure-Gradient Turbulent Boundary Layer Flow* (Royal Institute of Technology) (<http://www.diva-portal.org/smash/get/diva2:8624/FULLTEXT01.pdf>)
- [7] Degraaff D B and Eaton J K 2000 Reynolds-number scaling of the flat-plate turbulent boundary layer *J. Fluid Mech.* **422** 319–46
- [8] Schlatter P, Orlu R, Li Q, Brethouwer G, Fransson J H M, Johansson A V, Alfredsson P H and Henningson D S 2009 Turbulent boundary layers up to  $Re_\theta = 2500$  studied through simulation and experiment *Phys. Fluids* **21** 051702
- [9] Hutchins N, Chauhan K, Marusic I, Monty J and Klewicki J 2012 Towards reconciling the large-scale structure of turbulent boundary layers in the atmosphere and laboratory *Boundary-layer Meteorol.* **145** 273–306
- [10] Spalart P 1988 Direct simulation of a turbulent boundary layer up to  $Re_\theta = 1410$  *J. Fluid Mech.* **187** 61–98
- [11] Smagorinsky J 1963 General circulation experiments with the primitive equations: I the basic experiment *Monthly Weather Rev.* **91** 99–164
- [12] Deardorff J W 1970 A numerical study of three-dimensional turbulent channel flow at large Reynolds numbers *J. Fluid Mech.* **41** 453–80
- [13] Germano M, Piorelli U, Moin P and Cabot W H 1991 A dynamic subgrid-scale eddy viscosity model *Phys. Fluids A* **3** 1760–5
- [14] Moin P, Squires W, Cabot W and Lee S 1991 A dynamic subgrid-scale model for compressible turbulence and scalar transport *Phys. Fluids A* **3** 2746–57
- [15] You D and Moin P 2007 A dynamic global-coefficient subgrid-scale eddy-viscosity model for large-eddy simulation in complex geometries *Phys. Fluids* **19** 065110
- [16] Lesieur M, Metais O and Comte P 2008 *Large-Eddy Simulation of Turbulence* (Cambridge: Cambridge University Press)
- [17] Boris J P, Grinstein F F, Oran E S and Kolbe R L 1992 New Insights into large eddy simulation *Fluid Dyn. Res.* **10** 199–228
- [18] Garnier E, Mossi M, Sagaut P, Comte P and Deville M 1999 On the use of shock-capturing schemes for large-eddy simulation *J. Comput. Phys.* **153** 273–311
- [19] Hirt C W 1968 Heuristic stability theory for finite-difference equations *J. Comput. Phys.* **2** 339–55
- [20] Woodward P R and Colella P 1984 The numerical simulation of two dimensional fluid flow with strong shocks *J. Comput. Phys.* **54** 115–73
- [21] Smolarkiewicz P K and Margolin L G 1998 MPDATA: a finite-difference solver for geophysical flows *J. Comput. Phys.* **140** 459–80
- [22] Schlatter P and Orlu R 2012 Turbulent boundary layers at moderate Reynolds numbers: inflow length and tripping effects *J. Fluid Mech.* **710** 5–34
- [23] Collis S S and Chang Y 2002 The DG/VMS method for unified turbulence simulation *32nd AIAA Fluid Dynamics Conf. and Exhibit (St. Louis, MO)* pp 24–7
- [24] Sengupta K, Mashayek F and Jacobs G 2007 Large-eddy simulation using a discontinuous Galerkin spectral element method *45th AIAA Aerospace Sciences Meeting and Exhibit (Reno, NV)* pp 8–11
- [25] Wei L and Pollard A 2011 Direct numerical simulation of compressible turbulent channel flows using the discontinuous Galerkin method *Comput. Fluids* **47** 85–100
- [26] Uranga A, Persson P O, Drela M and Peraire J 2011 Implicit large eddy simulation of transition to turbulence at low Reynolds numbers using a discontinuous Galerkin method *Int. J. Num. Methods* **87** 232–61
- [27] Beck A D, Gassner G J and Munz C D 2014 *Spectral and High Order Methods for Partial Differential Equations—ICOSAHOM 2012 (Lecture Notes in Computational Science and Engineering)* ed M Azañez et al (Cham: Springer) pp 145–55
- [28] Bassi F, Botti L, Colombo A, Crivellini A, Ghidoni A and Massa F 2016 On the development of an implicit high-order discontinuous Galerkin method for DNS and implicit LES of turbulent flows *Eur. J. Mech. B* **55** 367–79
- [29] Fernandez P, Nguyen N C, Roca X and Peraire J 2016 Implicit large-eddy simulation of compressible flows using the Interior embedded discontinuous Galerkin method *54th AIAA Aerospace Science Meeting (San Diego, CA)* pp 1–15
- [30] Wiart C C, Hillewaert K, Bricteux L and Winckelmans G 2015 Implicit LES of free and wall-bounded turbulent flows based on the discontinuous Galerkin/symmetric interior penalty method *International J. Numer. Methods Fluids* **78** 335–54
- [31] Roth J R, Sherman D M and Wilkinson S P 2000 Electrohydrodynamic flow control with a glow discharge surface plasma *AIAA J.* **38** 1166–72

- [32] Debiassi M and Samimy M 2004 Logic-based active control of subsonic cavity flow resonance *AIAA J.* **42** 1901–9
- [33] Riherd M, Roy S and Visbal M 2011 Numerical investigation of serpentine plasma actuators for separation control at low Reynolds number *41st AIAA Fluid Dynamics Conf. and Exhibit (Honolulu, HI)* (<https://doi.org/10.2514/6.2011-3990>)
- [34] Gupta A D and Roy S 2014 Noise control of subsonic cavity flows using plasma actuated receptive channels *J. Phys. D: Appl. Phys.* **47** 502002
- [35] Jousset R, Weber R, Leroy A and Hong D 2013 Transition control using a single plasma actuator *Int. J. Aerosp. Eng.* **3** 26–46
- [36] Grundmann S and Tropea C 2007 Experimental transition delay using glow-discharge plasma actuators *Exp. Fluids* **42** 653–7
- [37] Simon B, Schnabel P and Grundmann S 2016 IR measurements for quantification of laminar boundary layer stabilization with dbd plasma actuators *New Results in Numerical and Experimental Fluid Mechanics X* (Berlin: Springer) pp 269–78
- [38] Porter C, McLaughlin T, Enloe C L, Font G, Roney J and Baughn J W 2007 Boundary layer control using a DBD plasma actuator *45th AIAA Aerospace Sciences Meeting and Exhibit (Reno, NV)* (<https://doi.org/10.2514/6.2007-786>)
- [39] Seraudie A, Aubert E, Naudé N and Cambronne J 2006 Effect of plasma actuators on a flat plate laminar boundary layer in subsonic conditions *3rd AIAA Flow Control Conf. (San Francisco, California)* (<https://doi.org/10.2514/6.2006-3350>)
- [40] Roy S and Wang C C 2008 Bulk flow modification with horseshoe and serpentine plasma actuators *J. Phys. D: Appl. Phys.* **42** 032004
- [41] Riherd M and Roy S 2013 Serpentine geometry plasma actuators for flow control *J. App. Phys.* **114** 083303
- [42] Ducros F, Comte P and Lesieur M 1996 Large-eddy simulation of transition to turbulence in a boundary layer developing spatially over a flat plate *J. Fluid Mech.* **326** 1–36
- [43] Israeli M and Orszag S A 1981 Approximation of radiation boundary conditions *J. Comput. Phys.* **41** 115–35
- [44] Bodony D J 2006 Analysis of sponge zones for computational fluid mechanics *J. Comput. Phys.* **212** 681–702
- [45] Choi H and Moin P 2012 Grid-point requirements for large eddy simulation: Chapman's estimates revisited *Phys. Fluids* **24** 011702
- [46] Van Driest E R 1951 Turbulent boundary layer in compressible fluids *J. Aerosol Sci.* **18** 145–60
- [47] Roupasov D V, Nikipelov A A, Nudnova M M and Starikovskii A Y 2009 Flow separation control by plasma actuator with nanosecond pulsed periodic discharge *AIAA J.* **47** 168–85
- [48] Li Y, Zhang X and Huang X 2010 The use of plasma actuators for bluff body broadband noise control *Exp. Fluids* **49** 367–77
- [49] Maden I, Kriegseis J, Maduta R, Jakirlic S, Schwarz C, Grundmann S and Tropea C 2012 Derivation of a plasma-actuator model utilizing quiescent-air PIV data *Proc. 20th Annual Conf. CFD Society (Alberta, Canada)*
- [50] Singh K P and Roy S 2008 Force approximation for a plasma actuator operating in atmospheric air *J. Appl. Phys.* **103** 013305
- [51] Benard N and Moreau E 2014 Electrical and mechanical characteristics of surface AC dielectric barrier discharge plasma actuators applied to airflow control *Exp. Fluids* **55** 1846
- [52] Thomas F O, Corke T C, Iqbal M, Kozlov A and Schatzman D 2009 Optimization of dielectric barrier discharge plasma actuators for active aerodynamic flow control *AIAA J.* **47** 2169
- [53] Moura R C, Mengaldo G, Peiró J and Sherwin S J 2017 On the eddy-resolving capability of high-order discontinuous Galerkin approaches to implicit LES/under-resolved DNS of Euler turbulence *J. Comput. Phys.* **330** 615–23
- [54] Wu X and Moin P 2009 Direct numerical simulation of turbulence in a nominally zero-pressure-gradient flat-plate boundary layer *J. Fluid Mech.* **630** 5–41
- [55] Schlatter P and Orlu R 2010 Assessment of direct numerical simulation data of turbulent boundary layers *J. Fluid Mech.* **659** 116–26
- [56] Sayadi T, Hamman C W and Moin P 2013 Direct numerical simulation of complete H-type and K-type transitions with implications for the dynamics of turbulent boundary layers *J. Fluid Mech.* **724** 480–509
- [57] Mansour N N, Kim J and Moin P 1988 Reynolds-stress and dissipation-rate budgets in a turbulent channel flow *J. Fluid Mech.* **194** 15–44
- [58] Elofsson P A and Alfredsson P H 2009 An experimental study of oblique transition in a Blasius boundary layer flow *Eur. J. Mech. B* **19** 615–36
- [59] Elofsson P A and Alfredsson P H 1998 An experimental study of oblique transition in plane Poiseuille flow *J. Fluid Mech.* **358** 177–202
- [60] Berlin S, Wiegel M and Henningson D S 1999 Numerical and experimental investigations of oblique boundary layer transition *J. Fluid Mech.* **393** 23–57
- [61] Laurien E and Kleiser L 1989 Numerical simulation of boundary-layer transition and transition control *J. Fluid Mech.* **199** 403–40
- [62] Rist U and Fasel H 1995 Direct numerical simulation of controlled transition in a flat-plate boundary layer *J. Fluid Mech.* **298** 211–48
- [63] Schmid P J and Henningson D S 1992 A new mechanism for rapid transition involving a pair of oblique waves *Phys. Fluids A* **4** 1986–9
- [64] Ryu S, Marxen O and Iaccarino G A 2015 Comparison of laminar-turbulent boundary-layer transitions induced by deterministic and random oblique waves at Mach 3 *Int. J. Heat Fluid Flow* **56** 218–32
- [65] Chang C L and Malik M R 1994 Oblique-mode breakdown and secondary instability in supersonic boundary layers *J. Fluid Mech.* **273** 323–60
- [66] Lumley J L 1967 The structure of inhomogeneous turbulent flows *Atmos. Turbul. Radio Wave Propag.* **790** 166–78
- [67] Berkooz G, Holmes P and Lumley J L 1993 The proper orthogonal decomposition in the analysis of turbulent flows *Ann. Rev. Fluid Mech.* **25** 539–75
- [68] Sirovich L 1987 Turbulence and the dynamics of coherent structures. I Coherent structures *Q. Appl. Math.* **45** 561–71
- [69] Barlow R S and Johnston J P 1988 Structure of a turbulent boundary layer on a concave surface *J. Fluid Mech.* **191** 137–76
- [70] Kim J, Moin P and Moser R 1987 Turbulence statistics in fully developed channel flow at low Reynolds number *J. Fluid Mech.* **177** 133–66